Geophysical Journal International

Geophys. J. Int. (2024) **237,** 109–122
Advance Access publication 2024 January 22
GJI Seismology

https://doi.org/10.1093/gji/ggae032

Deciphering the low-frequency seismic signals in the Weiyuan Shale gas field: implications for reservoir and structural heterogeneity

Aqeel Abbas [1], Hongfeng Yang [1,2,3] and Jinping Zi [1]

[1] *Earth and Environmental Sciences Programme, The Chinese University of Hong Kong, Hong Kong S.A.R.* 000000, *China. E-mail: hyang@cuhk.edu.hk*
[2] *Shenzhen Research Institute, The Chinese University of Hong Kong, Shenzhen, Guangdong* 518057, *China*
[3] *Institute of Environment, Energy and Sustainability, The Chinese University of Hong Kong, Hong Kong S.A.R.* 000000, *China*

Accepted 2024 January 18. Received 2024 January 9; in original form 2023 August 22

SUMMARY

Hydraulic fracturing (HF) often stimulates the local earthquake productivity which provides a unique opportunity to characterize the crustal heterogeneities, reservoir properties and fluid injection effects. However, the velocity models acquired solely based on the arrival time records are often undermined due to the seismic network coverage and interpolation techniques. Instead, we adopt the waveform-based approach to apprehend; (1) structural heterogeneities, (2) reservoir distribution and (3) signatures of the injected fluid in the Weiyuan shale gas field. We categorize the waveforms into dominant high and low frequencies based on the qualitative inspection and frequency index analysis of the seismic waveforms. We first inspect the waveform to access the potential controlling mechanisms (source, site and path effects) at both single and multiple stations in different azimuthal orientations. As a result, we find the path effect as a dominant factor to influence the waveform characteristics, for example *S*-wave amplitude, and frequency. Subsequently, to localize the path effect, we conduct an in-depth examination of events within 10 km of each seismic station and classify the waveform records using their frequency indices. Notably, certain stations record a significant proportion of low-frequency waveforms (LFWs, up to 20 per cent), while others have limited occurrences (∼1 per cent) indicating suspected anomalous zones. Afterward, we identify two suspected anomalous zones based on LFWs intensity and ray tracing map. Both zones are in close proximity to fault zones and preserved reservoirs with no HF activities, where fault damage zones or the fluid-rich reservoir may contribute to our observed LFWs.

Key words: Body waves; Induced seismicity; Wave propagation.

1 INTRODUCTION

In recent years, there has been a significant increase in exploitation activities targeting unconventional low-permeability reservoirs with advanced techniques, for example horizontal drilling and hydraulic fracturing (HF). During the HF process, a large volume of high-pressure fluid is used to create the fractures to enhance reservoir production at an economical scale. This permeability-enhancing technique has the capability to induce damaging earthquakes by a variety of mechanisms, including increased pore pressure due to fluid diffusion, poroelasticity effect, Coulomb stress transfer due to both earthquakes and aseismic slip (Ellsworth 2013; Eyre *et al.* 2019; Ge & Saar 2022; Yang *et al.* 2023). For instance, felt earthquakes associated with HF have been reported worldwide, for example in Canada (Wang *et al.* 2020a), the United Kingdom (Clarke *et al.* 2014), and China (Lei *et al.* 2017; Yang *et al.* 2020; Wong *et al.* 2021; Zi *et al.* 2023). Among the aforementioned regions, a substantial number of intense earthquakes ($M_L \geq 4$) have been documented in shale gas blocks in Western Canada Sedimentary Basin (Mahani *et al.* 2017; Wang *et al.* 2017; Atkinson *et al.* 2020), South Texas, USA (Fasola *et al.* 2019) and the Sichuan basin, Southwestern China (Lei *et al.* 2020; Yi *et al.* 2020).

Although disastrous from a hazard point of view, such intense seismic activities provide excellent opportunities to study the crustal structure, including fractures and faults distribution (Barthwal & van der Baan 2019; Long *et al.* 2020; Zhang *et al.* 2020), reservoir properties (Saenger *et al.* 2009; Zhang *et al.* 2009; Tselentis *et al.* 2011), and possible effects of HF activities, including fracture growth and fluid accumulation (Tan *et al.* 2023; Zi *et al.* 2023). For this purpose, seismic tomography methods, as powerful tools in revealing subsurface structures, have been widely adopted in preceding studies. However, the resolution of acquired results is often undermined by the limited coverage of seismic network and linear interpolation techniques (Miyazawa & Kato 2004; Liu & Gu 2012).

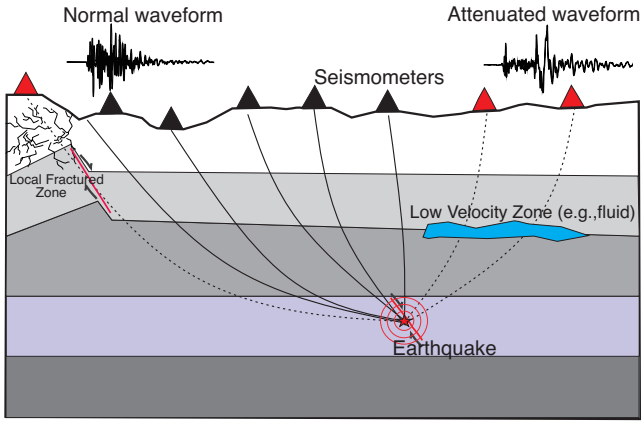

Figure 1. Schematic diagram representing the ray paths after an earthquake. Dotted lines represent the ray paths that encounter the low-velocity zones. The black and red triangles refer to stations with normal and attenuated waveforms, respectively.

Consequently, the resulting resolution (i.e. 5–10 km and 2–3 km in the horizontal and vertical directions, respectively) is insufficient to distinguish localized anomalous bodies such as fault damage zones, injected fluids or thin reservoir layers that may be up to a few hundred metres.

On the other hand, waveform attributes, including amplitude, phase, arrival time and frequency content are more sensitive to lithology, rock texture, pore fluid and temperature (Simm *et al.* 2014; Fawad *et al.* 2020) and are considered to be direct indicators of structural heterogeneities and different rock properties than velocity (Kita *et al.* 2014). Therefore, extracting such valuable information from the seismic waveforms could provide critical insights into subsurface structures, temporal velocity variation in fault zones (Baisch & Bokelmann 2001; Yang & Zhu 2010; Hung *et al.* 2022; Luan *et al.* 2022), and the characterization of hydrocarbon reservoirs (Shapiro *et al.* 2004; Maxwell & Urbancic 2005). For example, diffracted *S* waves and the delay time of *P*- and *S*-wave arrivals have been used to analyse the narrow low-velocity fault zone structures (∼150–200 m width) along the San Jacinto Fault Zone (SJFZ) in Southern California (Yang & Zhu 2010; Yang *et al.* 2014). Similarly, the observed amplification of seismic waveforms was found to be well correlated with known crustal structures and sedimentary basins across USArray (Bowden *et al.* 2017). Such amplified ground motion features also helped to delineate the low-velocity zone (LVZ) with high resolution across the Chenghai Fault Zone, Binchuan, Yunnan Province, China (Song & Yang 2022). Yang *et al.* (2018) noted distinct temporal variations in seismic velocity (5–20 per cent) that are consistent with groundwater level and reflect subtle stress changes near the Xiaojiang Fault Zone in Xundian County, Yunnan Province, China. In addition, waveforms inspection becomes a reliable and quick tool to verify the clock status on seismic stations using local and teleseismic events (Zhu *et al.* 2019; Abbas *et al.* 2023). Fig. 1 illustrates the possible impact of a fractured zone and a low-velocity body on the recorded waveforms in terms of decay in amplitude and frequency components.

The Sichuan basin has complex patterns of sedimentary formations with numerous shallow faults due to its multistage tectonic history and resultant structural deformations (Liu *et al.* 2021a; Fan *et al.* 2022). In recent years, it has experienced an abrupt increase in seismicity near hydraulic fracturing sites, accompanied by a rise in seismic hazards due to their shallow depth. For instance, the Weiyuan shale gas field (WSGF), located in the southwestern Sichuan Basin, has experienced 8 earthquakes with $M_w \geq 4$ since 2015. Among them, six events are located near the Molin fault at shallow depths, which is one of the major reasons why these earthquakes are so destructive (Yang & Yao 2021). To infer which seismogenic mechanisms and responsible faults could have triggered earthquakes, high-resolution subsurface structural information is indispensable. Several studies have been done in the WSGF to better delineate the crustal structures using seismic tomography (Zeng *et al.* 2020; Zi *et al.* 2023) but encountered limited resolution as mentioned above. Therefore, analysis of seismic attributes is of great significance in terms of studying the subsurface structures and their traces (e.g. faults and fractures) and the characterization of hydrocarbon reservoirs.

In addition, such complex deformation with extensive fractures is suitable for accumulating the injected fluid during HF operations. Recent studies show that a substantial amount of the injected fluid volume is retained (up to 75 per cent) in fractured shale reservoirs or hosted by nearby fractures (Makhanov *et al.* 2014) which poses significant economic, technical, and environmental concerns, including delayed triggering earthquakes on basement faults or water contamination in the future. Yet tracking the injected fluids underground remains challenging for the assessment of associated seismic risks because of the aforementioned limitations of seismic tomography. Therefore, it is important to track the mobility of injected fluid and inspect any temporal and spatial signatures of fluid on the waveform data near HF sites in addition to structural heterogeneities.

In this study, we examine the newly published seismic catalogue with good temporal and spatial coverage from the 23 permanent stations and 50 short-period temporary stations in the WSGF (Zi *et al.* 2023). This catalogue provides a unique opportunity to characterize crustal heterogeneities, reservoir properties and possible fluid injection effects based on qualitative (waveform inspection) and quantitative analysis (frequency index method). We first evaluate the waveforms to assess the potential controlling mechanisms (source, site and path effects) that significantly affect the waveform's attributes including amplitude and frequency content. This assessment covers both individual and multiple stations oriented at different azimuths. Subsequently, we conduct an in-depth examination of events and classify the waveform record into low and high frequencies using the frequency index method. Finally, we identify two suspected low-velocity anomalous zones surrounded by local fault structures and HF pads based on the ray path density. In addition, this study emphasizes the importance of waveform analysis using dense seismicity to comprehend the underlying controlling mechanisms and variations in local structures.

2 DATA DESCRIPTION

The WSGF is one of China's national demonstration areas for shale gas development in the Sichuan Basin (Fig. 2a). A prominent geological feature in this area is the Weiyuan anticline, a dome structure that extends in the northeast-to-southwest direction. On the north flank, numerous mapped faults trend towards the northeast, while the south flank features several faults, including the Molin fault, which trends southeastward (Yang *et al.* 2020; Liu *et al.* 2023). Before mid-2015, this region was considered to be stable in terms of low seismicity (Lei *et al.* 2020) with a total of 33 wells in the Changning–Weiyuan area (Tian *et al.* 2015). From then on, to raise the production of shale gas in the WSGF, more than 400 horizontal wells were deployed by the end of October 2020 (Liu *et al.* 2021b),

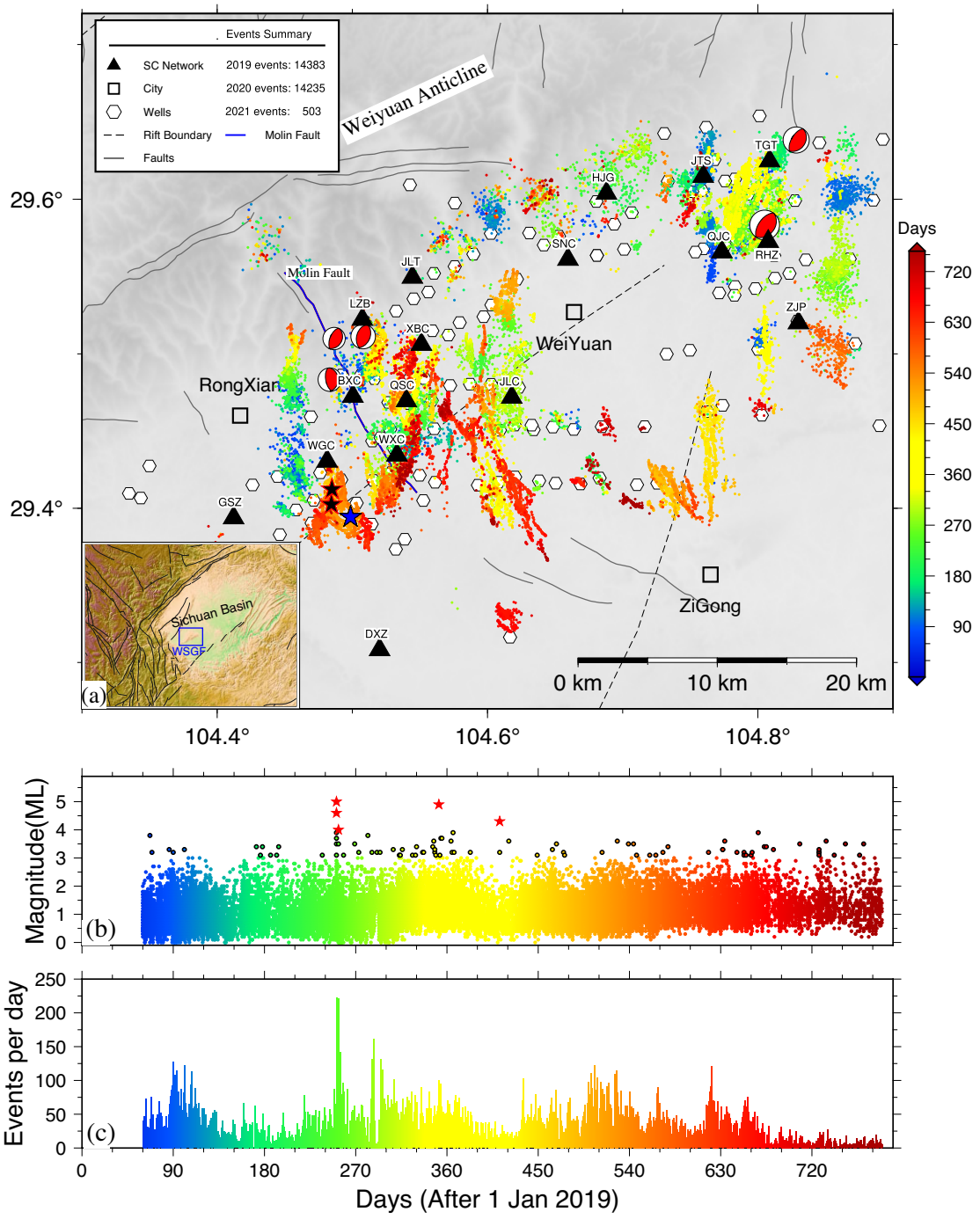

Figure 2. (a) Permanent seismic stations and relocated seismicity from March 2019 to February 2021 in the Weiyuan shale gas field (WSGF). Black triangles and white hexagons refer to seismic stations and HF platforms, respectively. Focal mechanisms of $M_L \geq 4$ in the catalogue are drawn (Zi *et al.* 2023). The inset shows the location of the Sichuan basin while WSGF is shown in blue rectangles. Black and blue stars refer to events, used in Figs 4 and 5, respectively. (b) The magnitude of daily earthquakes. Red stars and black circles refer to events with magnitudes greater than four and three, respectively. (c) Total number of daily events in the current catalogue after 1 January 2019.

which boosted the gas volume to a total of 53.87×10^8 m^3. On the other hand, it leads to a drastic increase in seismicity with a few damaging events (Fig. 2), including two events with M_w 4.3 and 5.2 in February and September 2019, respectively, which led to four fatalities, 75 injuries and an estimated economic loss of ∼10 million U.S. dollars (Yang *et al.* 2020; Yi *et al.* 2020; Wang *et al.* 2020b; Sheng *et al.* 2022). A recent study by Zi *et al.* (2023) reported a catalogue of ∼32 000 well-located events within a period of 2 yr in the WSGF. Zhang *et al.* (2024) investigated the stress drop of nearly 12 000 earthquakes and found significant spatial heterogeneity across the WSGF.

To monitor the seismic activities and conduct a comprehensive seismic hazard assessment, a network of 23 permanent seismic stations was deployed by the Sichuan Earthquake Agency (SEA) with

an average interstation distance of 10 km. Each station was equipped with a velocity-type seismograph that was set with a sampling rate of 100 Hz. In this study, we utilize 17 permanent stations and the aforementioned relocated earthquake catalogue (∼32 000 events) from March 2019 to February 2021 with a magnitude range of M_L 0 to M_L 5.6 (∼M_W 5; Zi *et al.* 2023) as shown in Fig. 2.

The new catalogue was obtained by double-difference tomography using travel times recorded at permanent stations and a dense temporal network (Zi *et al.* 2023). Besides differential times of manually picked *P* and *S* arrivals, additional waveform cross-correlation differential times of *P* waves (0.05 s before and 0.65 s after) and *S* waves (0.1 s before and 1.9 s after) are included in the relocation, which largely enhances the catalogue accuracy. A bootstrap test, which relocates events 100 times with randomly resampled differential times, gives an estimated mean horizontal and vertical location standard deviation of 50 and 80 m, respectively. Temporal variations in seismicity and recorded event magnitudes are shown in Figs 2(b) and (c). This data set was chosen for its comprehensive coverage, high-resolution relocations and reliable magnitude estimations, which allowed us to conduct our analysis with high accuracy and confidence.

3 METHODOLOGY

3.1 A qualitative approach: waveforms inspection

It is a major challenge to separate the site, source, and path effects on seismic wavefields (Ferreira & Woodhouse 2007). The term 'site effect' refers to the amplification of seismic waves due to geological conditions, such as shallow sedimentary rocks or fault damage zones, a phenomenon that necessitates only a single seismic station for evaluation (Sebastiano *et al.* 2019). One method for quantifying site effects is to examine the consistency of the waveforms at a selected station across multiple events. If site effects have a significant impact on the waveform amplitude, one would anticipate highly correlated signals at a particular station. In order to examine the signature of each contributor in the seismic data, we specifically choose the station 'BXC' to investigate the event waveforms within a 10-km epicentral distance range. This station selection is based on its proximity to the Molin fault and the anticipation of observing potential site effects associated with the fault damage zone. The implementation of a 10 km threshold (an average interstation distance in the SEA network) allows for more precise localization of any suspected anomalies across the station. We select one month of data spanning from May to June 2020 based on the higher number of events per day and the availability of essential information from HF operations (e.g. active well location, fracturing time, amount of injected fluid, etc.) during this time. Such a cautious selection of data sets aids in distinguishing the potential impacts of any heterogeneities along the path (e.g. crustal structure, reservoirs or injected fluid) on the seismic waveforms.

3.2 A quantitative approach: frequency index analysis

Although our waveform inspection can show the distinct low-frequency *S* waves, manual assessment is time-consuming, prone to human errors and becomes particularly challenging with large data sets. To overcome this, it is imperative to utilize other techniques using waveform amplitude and frequency contents. An effective and viable approach in this context entails the automated classification of individual waveforms, employing a frequency metric known as the frequency index (FI; Buurman *et al.* 2006). FI has been extensively applied in numerous studies, especially in volcano regions to classify waveform types and describe their characteristics based on frequency content (Buurman *et al.* 2006; Greenfield *et al.* 2019; Song *et al.* 2023). This method utilizes the ratio of energy in high- and low-frequency windows. FI can be defined as:

$$\mathrm{FI} = \log_{10}\left(\frac{\overline{A_{\mathrm{upper}}}}{\overline{A_{\mathrm{lower}}}}\right), \tag{1}$$

where A_{upper} and A_{lower} refer to spectral energies across selected windows of upper and lower frequencies, respectively (Fig. 5). A negative value of FI suggests the waveform is dominant by low-frequency energy, while a positive FI reflects more energy in the high-frequency window. Waveforms with comparable energy in upper and lower-frequency windows will have a value close to zero.

4 RESULTS

4.1 A qualitative approach: waveforms inspection

We first analyse several event waveforms (Fig. S1) on station BXC, considering different magnitudes. After initial data processing which involves removing the mean and trend and applying band-pass filtering (0.5–20 Hz), we normalize the waveforms by their maximum value and align them with respect to the epicentral distance (Fig. 3). It appears that most of the waveforms manifest anticipated characteristics, including high frequency and short coda duration within the first 6 km (Fig. S2). In contrast, some events located within an epicentre distance of 8.5–10 km show a distinct change in *S* waves with dominant low frequency and longer coda compared to *P* waves (Fig. 3b). Meanwhile, at the same epicentral distance, other events exhibit very regular signals without any attenuated features (Fig. 3a). In addition, we do not observe any obvious magnitude dependence for both low and high-frequency waveforms.

To further investigate the possibility of site effects, we examine the event waveforms within the same period as BXC at two nearby stations: WGC and WXC. These stations are located at different azimuthal locations (Fig. 2). We find that WXC exhibits similar signatures of low-frequency waveforms (LFWs) at certain distances as BXC (Fig. S3). Since the waveforms are recorded at the same station, the waveform attenuation at specific distances should not be attributed to site effect. Instead, it should be associated with either the source effects or ray paths. Conversely, WGC does not record any LFWs within 10 km (Fig. S4).

To investigate the source effects, we analyse the waveforms from one earthquake that were recorded on all stations within the 10-km radius (Fig. 4). If the earthquake source plays a primary role, the attenuation impacts on waveforms should be nearly identical across all stations. However, the recorded waveforms manifest distinct dominant frequencies, with certain stations displaying low-frequency waveforms (LFWs) characterized by an extended *S*-wave coda, while others exhibit high-frequency waveforms (HFWs). For example, despite having similar epicentral distances, station BXC exhibits a dominant low-frequency component and a prolonged coda, while station GSZ evinces an impulsive waveform without a significant low-frequency signature. As such, we can exclude the source effects and thus believe that the frequency variations in S waves are caused by structures along their ray paths.

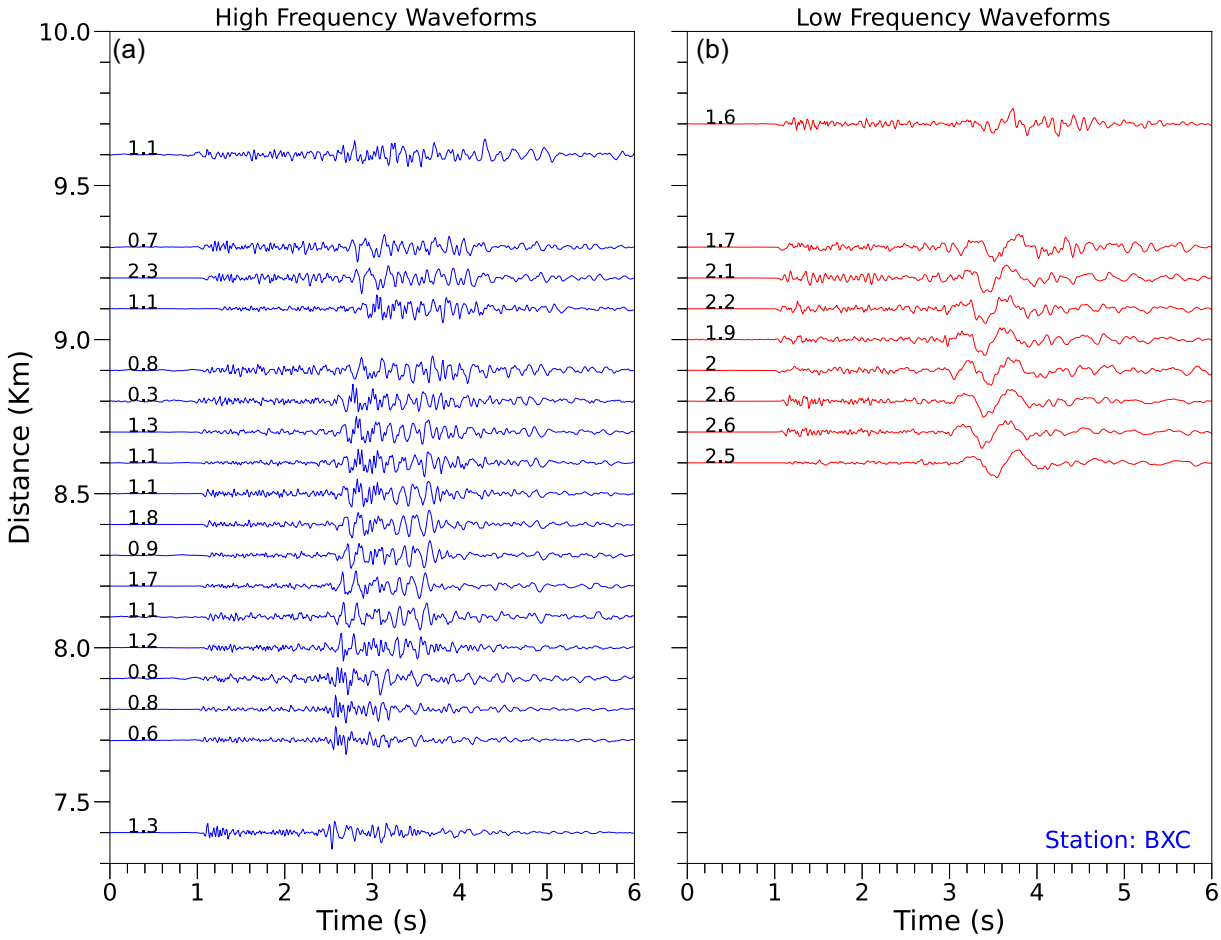

Figure 3. Recorded waveforms on station BXC within an epicentre range of 10 km. Black and red waveforms refer to events dominant with high and low frequency, respectively. Waveforms are aligned with respect to the *P* wave at 1 s. Numbers refer to the magnitude of each event recorded on this station.

4.2 A quantitative approach: frequency index analysis

We first analyse the two nearby events with M_L 2.6 (black stars in Fig. 2), recorded at a permanent station 'WXC' to set the FI threshold. The first event has a hypocentre depth of 3.29 km and is dominant with high-frequency components up to ∼12 Hz, while the second event, with a hypocentre depth of 3.75 km, manifests a significant attenuation of energy while propagating through the subsurface medium, with the prominent frequency content below 4 Hz (Fig. 5). These events exhibit qualitative similarities during the initial phases of *P* waves, but significant differences during *S* waves (Figs 5a and b). Based on the observed waveform's attributes, we select a 2.5-s window of *S* waves, including 0.5 s before and 2 s after their arrival (Fig. S5). *S* waves are chosen for their exceptional sensitivity to fluid and path effects, whereas the high velocity of *P* waves within a 10 km range renders them less optimal. However, combining the *P* and *S* waves window will also not influence significantly, but only *P* waves will present some biased results. Subsequently, we compute the FI for each waveform using eq. (1) with 0.5–3 Hz and 4–7 Hz as A_{lower} and A_{upper}, respectively. These specific frequency ranges have been identified as the most suitable for effectively distinguishing between LFWs and HFWs as shown in Figs 5(e) and (f).

On the manual comparison of the waveform's frequency spectrum and associated FI value (Figs S6 and S7), a criterion has been devised to accurately discern various earthquake waveforms, as illustrated in Fig. 6. For instance, we notice that waveforms with a dominant high-frequency content (above 5 Hz) consistently exhibit an FI value above 0.1, accounting for a significant proportion of all waveforms (70 273 waveforms, 79.35 per cent). Conversely, waveforms with a dominant low-frequency content (up to 4 Hz) exhibit FI value below −0.2, accounting for only 3.78 per cent (3344 waveforms) of the total waveforms. Furthermore, waveforms with uniform energy distribution or the absence of distinct frequency components have FI values between −0.2 and 0.1 (14 946 waveforms, 16.88 per cent). These waveforms pose a challenge in terms of their classification as either LFWs or HFWs, so we typically specify them as hybrid waveforms. All waveforms consistently adhere to the FI standard mentioned earlier, providing us with greater confidence in the reliability of these classifications for further analysis. In order to better constrain the regions responsible for LFWs, we first analyse the percentage of LFWs to HFWs at each station within a 10 km radius. Subsequently, we conduct an assessment of the cumulative count of LFWs and HFWs associated with each event to ascertain the predominant region exhibiting a higher prevalence of LFWs. This investigation aims to discern whether the observed

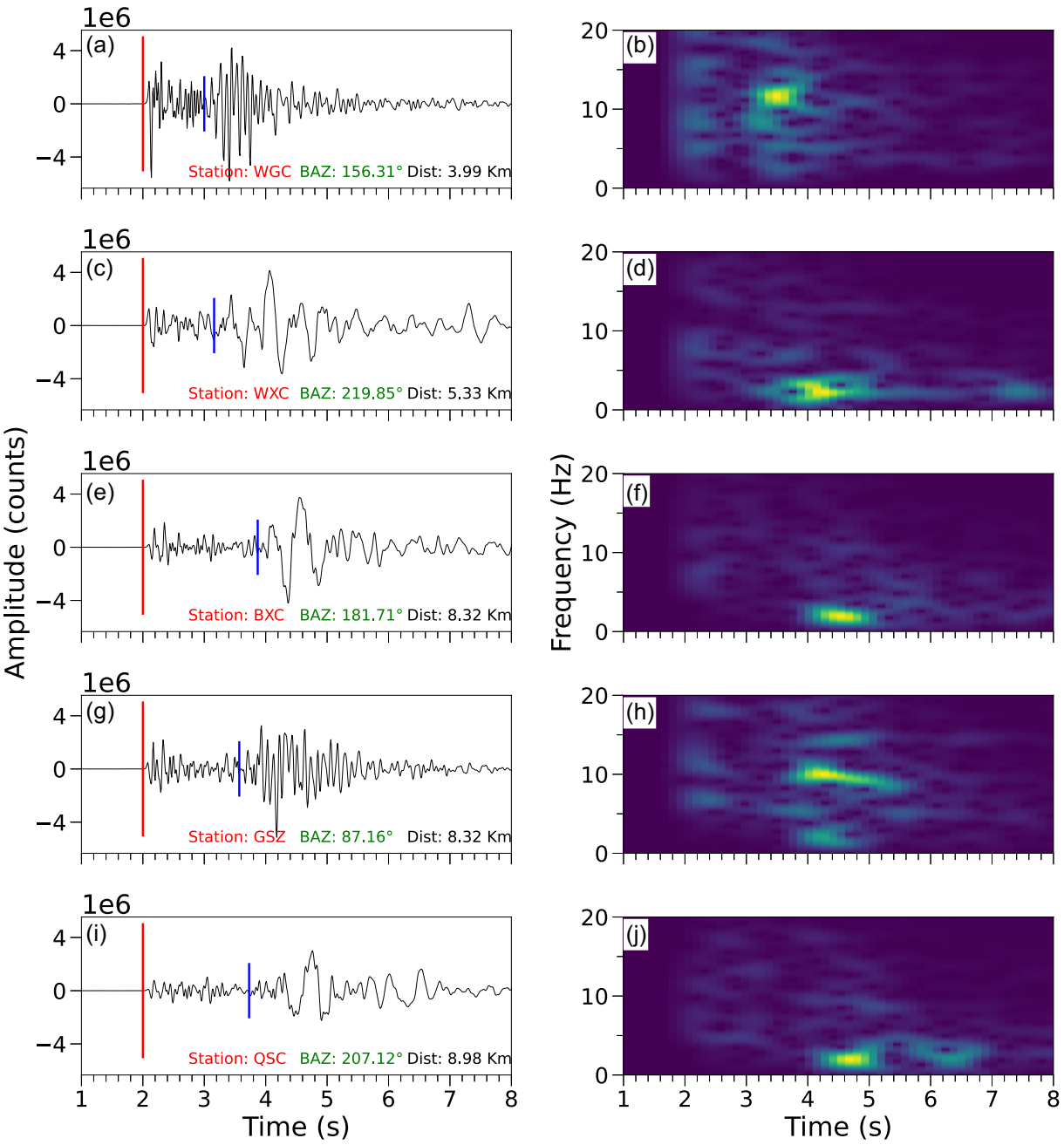

Figure 4. Event waveforms with the corresponding spectrogram recorded on nearby 5 stations within 10 km are plotted with increasing epicentre distance from top to bottom. The event was recorded on 26 May 2020. The red and blue bars refer to *P*- and *S*-wave arrivals, respectively. BAZ: backazimuth (°), Dist.: Epicentral distance (km).

LFWs exclusively arise from path effects or if any of the events are influenced by source mechanics.

4.2.1 FI analysis on each station

The cumulative number of observed LFWs and HFWs varies across each station in the study area (Table. S1). To comprehensively assess their distribution, we examine the percentage of total LFWs to HFWs at each station. These calculations unveil significant variations in the LFW/HFW percentage among stations, suggesting notable discrepancies in the influence of local geological factors from one station to another. For instance, some stations either do not record any LFW or have negligible LFW/HFW percentages (e.g. HJG, WGC). On the other hand, some stations record a high percentage (≥10 per cent) of LFW, e.g. WXC and GSZ as shown in Fig. 7.

Notably, the station WXC is one of the prominent stations with the highest number of LFWs (up to 20 per cent), located on the south section of the Molin fault. We have conducted a detailed comparative analysis of the LFWs and HFWs recorded at WXC and have examined their temporal and spatial distribution. Based on our analysis, we identify three distinct zones within a 10 km radius of the epicentre, each of which is characterized by either predominantly low or high frequencies waveforms as illustrated in

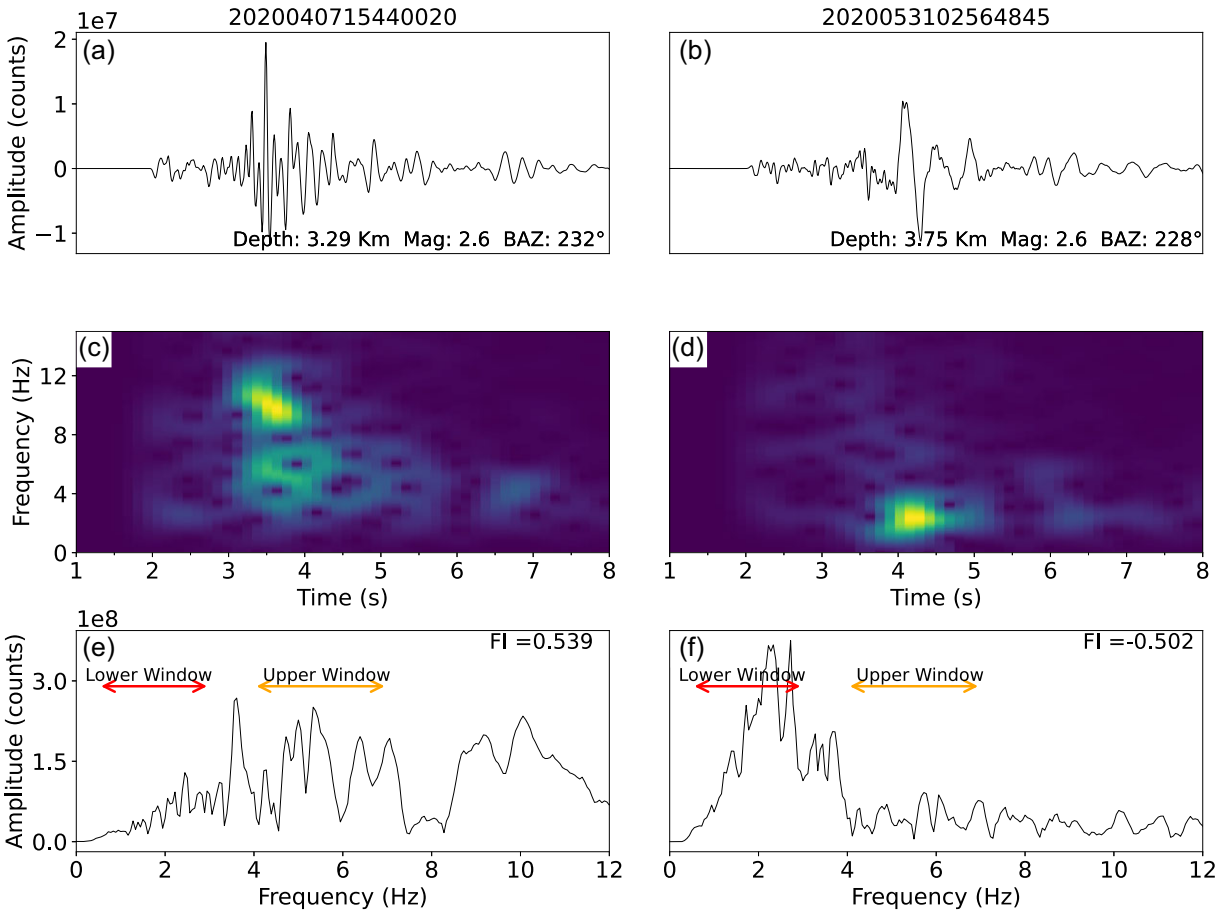

Figure 5. Comparison between (a–b) Seismic waveform, (c–d) Spectrogram and (e–f) frequency spectrum of a typical high-frequency (Event 1) and low-frequency event (Event 2). Arrows highlight the selected range of the upper and lower frequency windows for frequency index analysis. FI: the frequency index value for each waveform, Mag: Magnitude, Dist.: Epicentral distance.

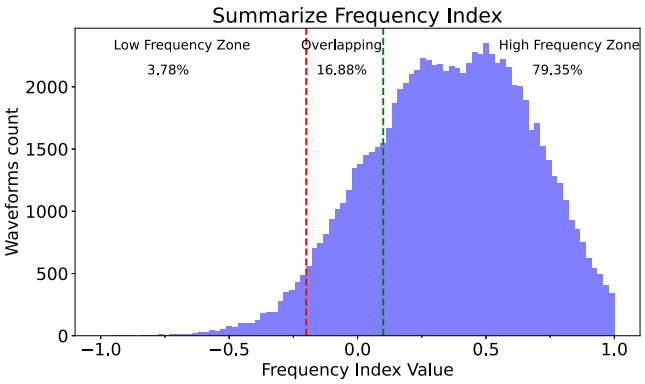

Figure 6. Frequency index value for each waveform in the catalogue based on defined selection criteria. Green and red lines separate the high and low-frequency zones, respectively, while the middle section refers to the uncertain classification of waveforms.

Fig. 8 (black circle and rectangle represent the dominant HFWs and LFWs zones, respectively). It is worth noting that areas displaying predominant LFWs are characterized by a conspicuous absence of HFWs within the same region, and conversely, regions with a substantial presence of HFWs exhibit a notable scarcity of LFWs. Our results consistently show the occurrence of both HFWs and LFWs, independent of spatial or temporal factors, indicating the existence of an enduring anomalous zone (Figs 8c and d).

4.2.2 FI analysis of each event

Considering the substantial number of LFWs at any station (e.g. WXC), it is a plausible assumption that local geology or other factors near the station may have a strong influence. For instance, if an event has only one associated LFW, it is difficult to distinguish whether it is due to local site effects or path effects. On the other hand, it is postulated that if multiple stations with wide azimuthal coverage record the LFWs from a single event, then the anomalous source is either in close proximity to the epicentre or has a widespread distribution in the study area.

To mitigate the potential influence of these localized factors, we examine each event and categorize them based on their associated LFWs. We find that events recorded on a minimum of one station within 10 km are uniformly distributed in the WSGF (Fig. 9a). Consequently, discerning the most prominent zone and comprehending the underlying controlling mechanism becomes challenging. In contrast, events associated with at least two LFWs are relatively infrequent, accounting for only 16 per cent of the total events with LFWs (2048) as illustrated in Fig. 9(b). This scarcity, instead of diminishing the significance, accentuates the presence of two distinct prominent zones with the highest occurrence (zone A and B). In zone A, the occurrence of LFWs is notably high, while in zone B, it is comparatively lower. Nevertheless, it is worth noting that two stations in Zone B, when compared to other stations in the WSGF, have recorded a percentage above 5 per cent, which is statistically

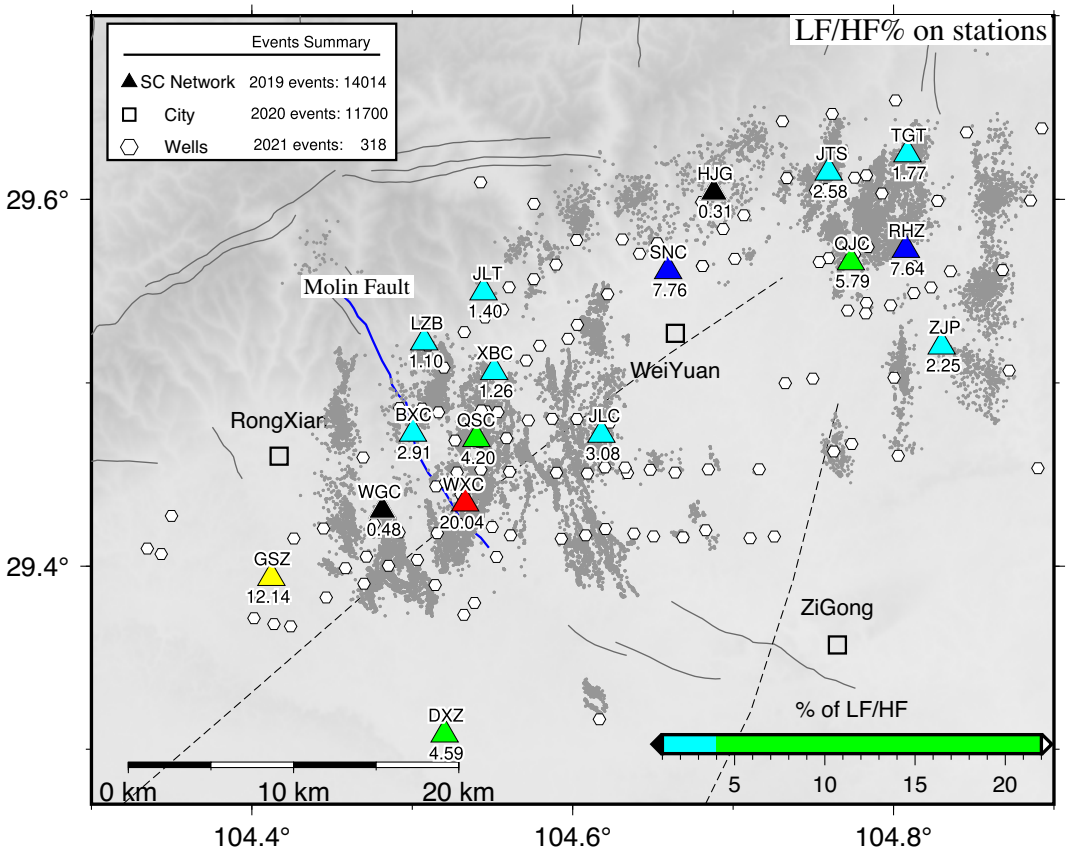

Figure 7. Percentage of low-frequency waveforms (LFWs) to high-frequency waveforms (HFWs) at each station (marked by triangles). Station names and corresponding LFW/HFW percentages are indicated above and below the station symbols, respectively. The black triangle denotes the stations with very rare LFWs (below 1 per cent). The grey circles refer to the total seismicity in the WSGF. Blue and black thin dashed lines refer to Molin Fault and Rift boundaries, respectively.

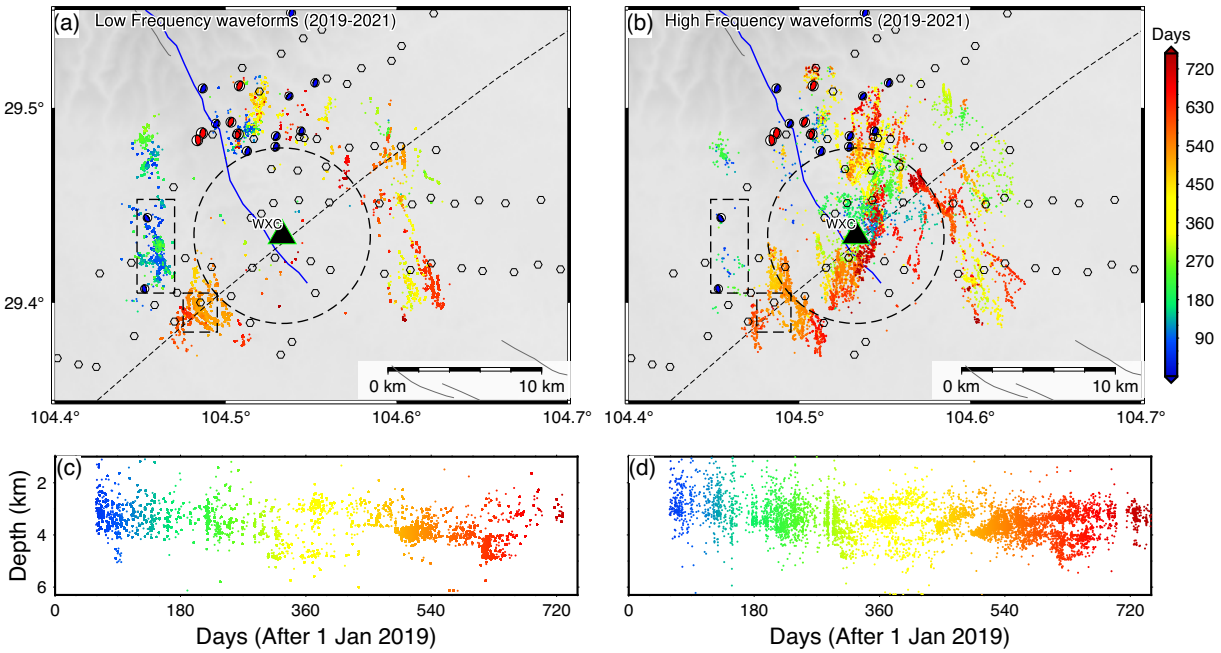

Figure 8. Temporal and spatial coverage of events on station WXC. (a–b) Low-frequency waveforms (LFWs) and high-frequency waveforms (HFWs) recorded on station WXC. LFWs and HFWs refer to the waveforms dominant with frequencies below and above 5 Hz, respectively. (c–d) Events distribution with respect to depth and number of days (from 1 January 2019). Black circle and rectangles illustrate the zones with dominant LFW or HFW, respectively.

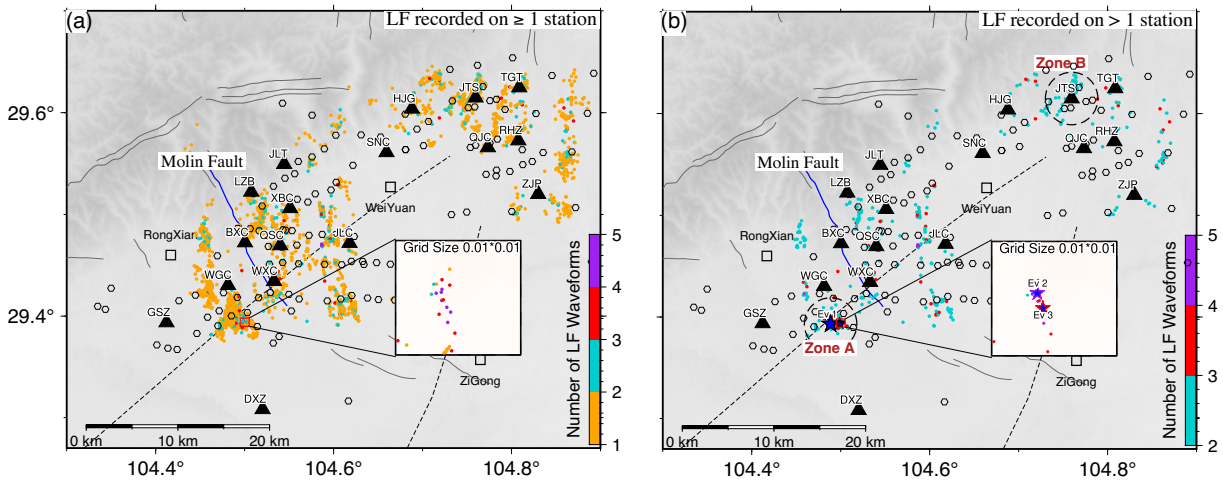

Figure 9. Location of low-frequency event waveforms recorded on different numbers of stations. (a) Any event depicts the low-frequency waveforms on any station and (b) more than one station. Events colours refer to the number of LFWs recorded on the total number of stations within 10 km. Three events (stars) are randomly selected events to verify the FI results. Inset: zoom out view (0.01° × 0.01°) from Shuangshi cluster highlighting the change in the number of LFW.

significant. Remarkably, within the observed events, only a few events demonstrate the utmost occurrence of five associated LFWs (Fig. 9, zoom view).

To verify the different number of LFWs associated with collocated events with FI values, we select three events within a grid size of 0.01° × 0.01° (Fig. 9b) and inspect the waveforms (Fig. 10). It shows that small spatial variation in hypocentres can lead to significant changes in the waveforms. Despite the variations in LFW distribution, no event emerges as dominant with low frequency across all stations, thereby indicating the absence of a singular low-frequency event within the given criteria. These waveforms are not limited to a single zone but are distributed throughout the WSGF (Figs S8–11).

To better visualize the spatial distribution of LFWs and HFWs, we evaluate the ray path coverage and analyse the ray hit count in grid size of 0.0125° × 0.00875° (Fig. 11). Distinct patterns in ray density of LFWs become evident (Figs 11a and b), identifying two regions with a higher concentration of ray paths similar to Fig. 9. In contrast, the ray density of HFW appeared to exhibit a relatively homogeneous distribution throughout the study region, suggesting a more uniform propagation behavior of high-frequency wave energy (Figs 11c and d). While there is an overlap in the ray paths depicted on the map view, it is important to acknowledge that collocated events exhibit distinct frequency responses due to slight depth variations as shown in Figs S8–11. It shows that these depth differences could contribute to discernible discrepancies, potentially explaining the possibility of observed anomalies.

5 DISCUSSION

5.1 Site and source effects

It is a growing approach to utilize the dense array seismic network to understand the seismic site response (Song & Yang 2022), estimation of fault damage zone (Zhang *et al.* 2022) and shallow velocity structures (She *et al.* 2022) but it requires extensive computational resources and data processing tools. The application of waveform analysis based on single stations can be an expeditious and cost-effective method for rapid assessment. The waveforms data set from the WSGF enables us to distinctly separate the possibility of site, source, and path effects using individual stations (WGC, BXC and WXC). The presence of attenuated waveforms at a certain distance supports the notion that site effects do not appear to be the leading physical mechanism driving the trends in our observations (Fig. 3). Furthermore, establishing a maximum distance threshold for event observation (set at 10 km in this study) aids us in the focused analysis of specific zones at predetermined distances. This approach reduces uncertainty by narrowing our examination to these targeted areas, rather than the entire study region.

Besides the typical HF-induced seismicity, Hybrid-frequency earthquakes have been reported as a new type of waveform that exhibits broader (long-period) body wave pulses and lower frequency coda on all stations (Bame & Fehler 1986; Hu *et al.* 2017; Yu *et al.* 2021). It is well established that if LFWs are cognate with the seismic rupture process (slower rupture speeds and lower stress drop values) (Niyogi *et al.* 2023), their low-frequency radiation pattern should be consistent on all stations. However, in this study, waveforms at different azimuths show considerable variations in seismic attributes, especially in amplitude and frequency. For instance, three out of five stations confined within a narrow azimuth range (180–220°), are deficits of high-frequency seismic radiation but prolonged coda waves. In contrast, the other two stations (WGC and GSZ) are considered to be normally induced events with high-frequency and less attenuated waveforms (Fig. 4). Contrary to reported low-frequency earthquakes in northeast British Columbia, Canada (Yu *et al.* 2021), such variations in dominant frequencies among the stations highlight the pronounced influence of azimuth and contradict source effects as the primary cause of LFWs. After excluding the site and source effects, such signatures provide robust evidence to further trace out any geological variation including the presence of low-velocity zones in the study area.

5.2 Possible source of low-velocity zone

The observed variations in percentiles of LFWs across stations, including those with near-zero LFW recordings, highlight the complex interplay of geological factors (Fig. 7). Similar LFWs behavior has been reported in several environments including coal mining

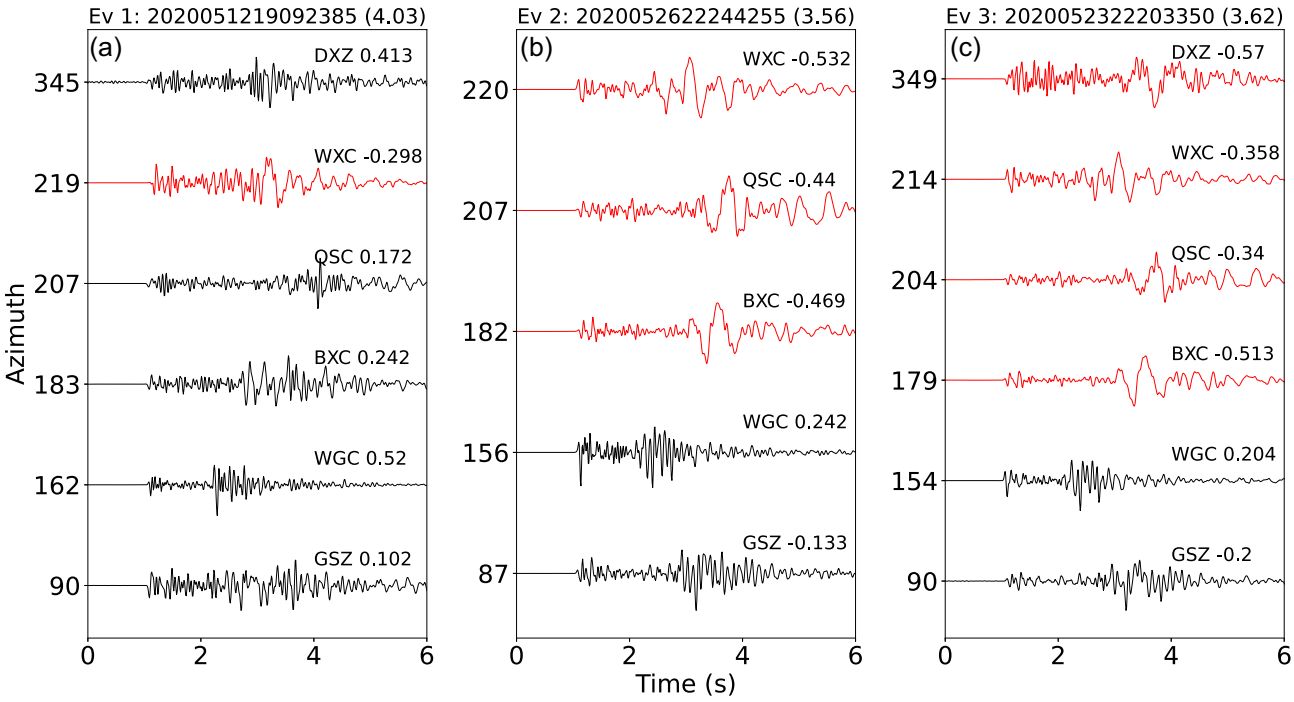

Figure 10. Waveforms of three collocated events (blue stars in Fig. 9b). Title of each subplot refers to 'event number: event ID (Depth)'. The station name and corresponding frequency index (FI) are mentioned for each waveform. Waveforms with dominant low frequency are highlighted with red colours.

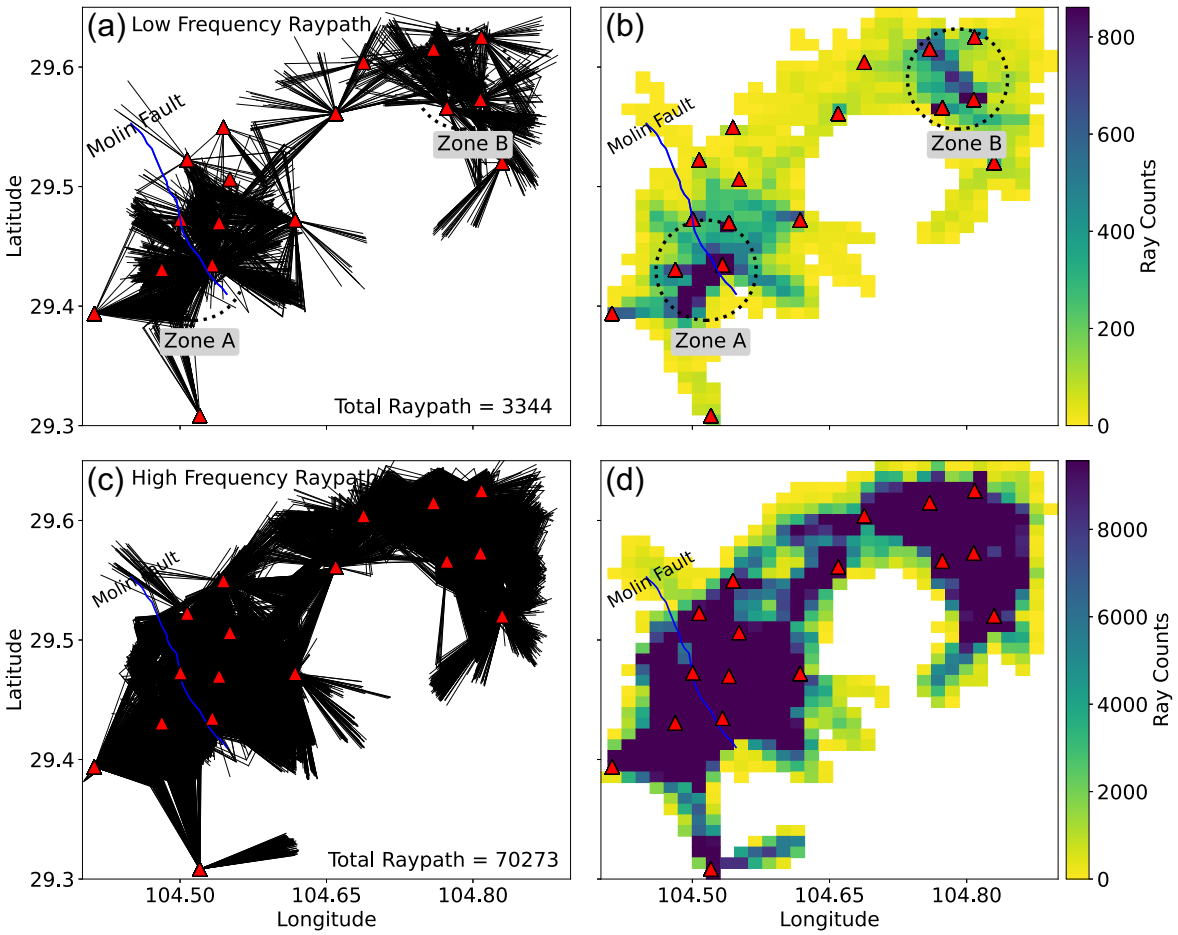

Figure 11. Ray tracing and ray counts of low-frequency waveforms (a–b) and high-frequency waveforms in the WSGF (c–d). The blue line refers to the Molin fault while red triangles represent the station location.

(Yu *et al.* 2022), HF activities (Yu *et al.* 2021), subduction zones (Gong & McGuire 2022), and volcanic regions (Harrington & Brodsky 2007) where either fluids or path effects account for such LFWs signatures. Likewise, our findings reiterate that distinct structural or other factors along the path in close proximity to the station govern the occurrence and characteristics of LWFs. For instance, the absence of an anomalous zone in the immediate vicinity of certain stations (HJG and WGC) may account for the nearly zero LFWs recordings and it further helps us to exclude such regions. On the other hand, several other stations show significant dominant LFWs ($\geq$2 per cent), particularly concentrated near the Molin Fault and in the northeastern part of WSGF. We suggest that localized structure deformation might be responsible for the high occurrence of LFWs along the Molin fault, especially at station WXC, which is located at the junction of the Molin fault and rift boundary. In addition, there is a notable contrast in the intensity of HF activities between the eastern and western zones of the Molin fault, indicating the preservation of the reservoir in a non-fracking zone. This observation becomes particularly evident in Fig. 8, where the absence of HF activities (preserved reservoir) between the station and two zones with dominant LFWs contributes to a higher percentage of LFWs recorded. The presence of highly attenuated *S* waves, further emphasizes the role of such preserved reservoirs in the occurrence of LFWs (Figs 3, S2 and S3). Our findings support that continuous detections of LFWs are highly attributed to preserved shale gas reservoirs or/and geological structures, notably the Molin fault. It is difficult to distinguish these two controlling factors because of the current network coverage with large interstation distance and limited information about the ongoing HF activities.

In the northeast of WSGF, four stations are closely located within an average interstation distance of 10 km. Among them, RHZ and QJC record $\geq$5 per cent of LFWs while the other two stations are confined to 2 and 1 per cent (Fig. 7). Contrary to associated LFWs near the Molin fault, we do not find any record of mapped fault structure in this zone. But this region witnessed two intense earthquakes with M_L 5.6 ($\sim M_w$ 5.0) and M_L 5.4 ($\sim M_w$ 4.9) in 2019 (Lei *et al.* 2020; Yi *et al.* 2020), which highlights the complex deformation including the existence of critically stressed faults. Similar to the western zone of the Molin fault, a 'seismicity gap' between station JTS and QJC is prominent where no HF wells and associated seismicity are recorded throughout the catalogue which refers to no production from the reservoir. Thus, the existence of a preserved reservoir is a common feature that may affect the waveforms significantly (Fig. 2).

5.3 Possible location of low-velocity zone

Event locations and their associated LFWs on nearby stations using FI are able to provide more constraints about the suspected anomalous zone. For instance, when one event is observed as LFW on several stations (Figs 4 and 10), two viable scenarios can account for significant attenuation on a broad azimuth range:

1.The source of LFWs is widely distributed in the region.
2.The source of LFWs is in close proximity to the epicentre.

However, recent tomography results do not support the existence of velocity variations on such a scale and mainly document the velocity variations along the Molin and basement rift faults (Zi *et al.* 2023). Consequently, their impact is anticipated to be confined to specific azimuths rather than exerting a widespread influence on waveforms across a broad azimuthal range. Instead, we infer that the anomalous zone is located close to the event epicentre if recorded on a wide azimuth scale (Fig. S12). To accurately pinpoint the location of the anomalous zone, a thorough analysis of events with multiple LFWs over a broad azimuth is crucial. However, it is challenging to analyse each event individually. Therefore, the distribution of events (Fig. 9) and ray-count density (Fig. 11) for both LFWs and HFWs provides a comprehensive overview of the possible location of such anomalous zones. These two anomalous zones are well supported by the existence of structural deformation and preserved reservoir. By conducting such analysis, we can infer that these LFWs signatures are not solely influenced by structural variations but are also potentially associated with anomalous bodies (gas packets or injected fluid) near the event epicentres in highlighted zones with dense LFW paths.

5.4 Significance of further investigations and proposed methodology

In this study, we use seismic attributes analysis to unveil subsurface anomalous zones that often elude detection by conventional seismic tomography models. However, a comprehensive analysis incorporating precise localization and characterization of these zones is indispensable for discerning the complex interplay of subsurface structures, preserved reservoirs, and HF activities. The current seismic network is hindered by its limited number of stations and extensive interstation distances, rendering it insufficient to accomplish this objective. Typically, within a 10 km radius, one would find a maximum of five stations with non-uniform deployment, resulting in clustering along specific azimuths. Simultaneously, the non-uniform distribution of seismic events in the study area can lead to unequal ray counts within grid cells, potentially affecting the accuracy and reliability of identified anomalous zones. To address this inherent limitation, we have deployed a dense seismic array comprising around $\sim$500 stations with an average interstation distance of $\sim$2 km. The resulting dense array configuration will facilitate enhanced spatial resolution and improved delineation of the anomalous zones, thereby providing invaluable insights into their geological characteristics and potential as hydrocarbon reservoirs.

Besides, studies have shown that changes in the physical state of rocks including fluid saturation (Murphy 1982; Yin *et al.* 1992; Muller *et al.* 2010) and the presence of fractures (Zhu *et al.* 2007; Chichinina *et al.* 2009) have a stronger effect on seismic attenuation than velocity. In the case of the HF experiment, Zhai *et al.* (2017) observed that the alteration of physical properties in host rock (Longmaxi shale) is not sufficient to affect the body-waves arrival times than seismic attenuation. Thereby, we suggest a critical improvement in current velocity tomography methods, which traditionally rely solely on arrival time information and do not utilize amplitude and frequency data. To refine the subsurface structural analysis, it is advantageous to incorporate both arrival times and frequency information, particularly through the utilization of the frequency index method. By embracing these approaches, our study contributes to a more comprehensive and accurate assessment of subsurface properties and anomalies.

5.5 Limitations

The current findings, based on the available data set, convincingly reveal the suspected low-velocity zones that were not evident in the present 3-D velocity model (Zi *et al.* 2023). However, it is essential

to acknowledge certain limitations inherent in the FI method employed. One notable constraint lies in the method's dependency on user-defined upper and lower frequency thresholds. This introduces a degree of subjectivity, particularly when applying the FI method to data sets originating from diverse study areas. Therefore, it is important to define an acceptable criterion to ensure the consistency and precision of the measurements derived from the FI method.

6 CONCLUSION

In this study, we demonstrate the effectiveness of waveform analysis to understand the subsurface structure and reservoir characteristics through induced seismicity. Distinct LFWs appear to be independent of source and site effects in the WSGF through qualitative waveform analysis. Our results highlight the two potential anomalous low-velocity zones, as determined by frequency index analysis and ray count map. These zones are in close proximity to the Molin fault and preserved reservoirs with no fracking so we infer that these LFWs are not solely affected by the reservoir but may also be associated with fault damage zones that exist along the ray path. Due to high sensitivity to fluid and structure variations, inspecting the seismic waveforms is expected to provide important constraints on the subsurface structures and reservoir heterogenies. However, precise identification and localization of the factors controlling such LFWs remain challenging due to the significant interstation distances. The construction of a dense seismic network is recommended to refine the spatial resolution of the suspected zones with less uncertainty. This study suggests the joint inversion in tomography models by utilizing both arrival times and frequency information for better structural constraints.

ACKNOWLEDGMENTS

The authors would like to thank the Editor Dr. Andrea Morelli, and two anonymous reviewers for helpful comments and constructive reviews. This work is supported by the National Natural Science Foundation of China (No. U2139203), Hong Kong Research Grant Council Grants (No. 14303721), Faculty of Science at The Chinese University of Hong Kong.

DATA AVAILABILITY

The data used in this paper will be shared on reasonable request to the corresponding author.

CONFLICT OF INTEREST

The authors acknowledge that there are no conflicts of interest recorded.

SUPPORTING INFORMATION

Supplementary data are available at *GJI* online.

Figure S1. Location of recorded low and high frequency waveforms on station BXC.
Figure S2. Recorded waveforms with good SNR on station BXC within an epicentre range of 10 km. Black and red waveforms refer to events dominant with high and low frequency, respectively. Waveforms are aligned with respect to the *P* wave at 1 s.
Figure S3. Recorded waveforms with good SNR on station WXC within an epicentre range of 10 km. Black and red waveforms refer to events dominant with high and low frequency, respectively. Waveforms are aligned with respect to the *P* wave at 1 s.
Figure S4. Recorded waveforms with good SNR on station WGC within an epicentre range of 10 km. Black and red waveforms refer to events dominant with high and low frequency, respectively. Waveforms are aligned with respect to the *P* wave at 1 s.
Figure S5. Events comparison using (a and b) seismic waveform and (c and d) frequency spectrum of selected *S*-wave windows for a typical high-frequency (Event 1) and low-frequency event (Event 2). Arrows highlight the selected range of the upper and lower frequency windows for frequency index analysis.
Figure S6. Normalized frequency spectrum and corresponding frequency index value of three events from northeastern Weiyuan (Events location are marked with stars in Fig. S8).
Figure S7. Normalized frequency spectrum and corresponding frequency index value of three events from northeastern Weiyuan (Events location are marked with stars in Fig. S8).
Figure S8. Selection of three group of events from different parts of WSGF. Numbers of stars refer to events number from each group in Figs S9, 10 and 11.
Figure S9. Selection of three collocated events from southwest of Molin Fault. Title of each subplot refers to 'event number: event ID (Depth)'. While station name and corresponding frequency index (FI) are mentioned for each waveform.
Figure S10. Selection of three collocated events from East of Molin Fault. While station name and corresponding frequency index (FI) are mentioned for each waveform.
Figure S11. Selection of three collocated events from northeast of WSGF. Title of each subplot refers to 'event number: event ID (Depth)'. While station name and corresponding frequency index (FI) are mentioned for each waveform.
Figure S12. Schematic diagram of possible location of suspected anomalous zone with respect to different number of LFWs associated with each event and station location. Dotted lines represent the ray paths that encounter the low-velocity zones. The black and red triangles refer to stations with normal and attenuated waveforms, respectively.
Table S1. Total number of recorded high, low and mixed frequency waveforms and their percentage (out of total recorded waveforms) on each station.

Please note: Oxford University Press are not responsible for the content or functionality of any supporting materials supplied by the authors. Any queries (other than missing material) should be directed to the corresponding author for the article.

REFERENCES

Abbas, A., Zhu, G., Zi, J., Chen, H. & Yang, H., 2023. Evaluating and correcting short-term clock drift in data from temporary seismic deployments, *Earthq. Res. Adv.,* **3,** 100199.
Atkinson, G.M., Eaton, D.W. & Igonin, N., 2020. Developments in understanding seismicity triggered by hydraulic fracturing, *Nat. Rev. Earth Environ.,* **1,** 264–277.
Baisch, S. & Bokelmann, G.H.R., 2001. Seismic waveform attributes before and after the Loma Prieta earthquake: scattering change near the earthquake and temporal recovery, *J. geophys. Res.,* **106,** 16 323–16 337.
Bame, D. & Fehler, M., 1986. Observations of long period earthquakes accompanying hydraulic fracturing, *Geophys. Res. Lett.,* **13,** 149–152.

Barthwal, H. & van der Baan, M., 2019. Passive seismic tomography using recorded microseismicity: application to mining-induced seismicity, *Geophysics,* **84,** B41–B57.

Bowden, D.C., Tsai, V.C. & Lin, F.-C., 2017. Amplification and attenuation across USArray using ambient noise wavefront tracking, *J. geophys. Res.,* **122,** 10 086–10 101.

Buurman, Helena & West, Michael E., 2006. Seismic precursors to volcanic explosions during the 2006 eruption of Augustine Volcano, in *The 2006 Eruption of Augustine Volcano, Alaska,* pp. 41–57, eds Power, J.A., Coombs, M.L. & Freymueller, J.T., U.S. Geological Survey Professional Paper 1769, USGS.

Chichinina, T., Obolentseva, I., Gik, L., Bobrov, B. & Ronquillo-Jarillo, G., 2009. Attenuation anisotropy in the linear-slip model: interpretation of physical modeling data, *Geophysics,* **74,** WB165–WB176.

Clarke, H., Eisner, L., Styles, P. & Turner, P., 2014. Felt seismicity associated with shale gas hydraulic fracturing: the first documented example in Europe, *Geophys. Res. Lett.,* **41,** 8308–8314.

Ellsworth, W.L., 2013. Injection-induced earthquakes, *Science,* **341**(6142), doi:10.1126/science.1225942.

Eyre, T.S., Eaton, D.W., Garagash, D.I., Zecevic, M., Venieri, M., Weir, R. & Lawton, D.C., 2019. The role of aseismic slip in hydraulic fracturing-induced seismicity, *Sci. Adv.,* **5**(8), doi:10.1126/sciadv.aav7172.

Fan, C.H. *et al.* 2022. Complicated fault characterization and its influence on shale gas preservation in the southern margin of the Sichuan Basin, China, *Lithosphere,* **2022**(Special 12), doi:10.2113/2022/8035106.

Fasola, S.L., Brudzinski, M.R., Skoumal, R.J., Langenkamp, T., Currie, B.S. & Smart, K.J., 2019. Hydraulic fracture injection strategy influences the probability of earthquakes in the Eagle Ford Shale play of South Texas, *Geophys. Res. Lett.,* **46,** 12 958–12 967.

Fawad, M., Hansen, J.A. & Mondol, N.H., 2020. Seismic-fluid detection—a review, *Earth Sci. Rev.,* **210,** doi:10.1016/j.earscirev.2020.103347.

Ferreira, A.M.G. & Woodhouse, J.H., 2007. Source, path and receiver effects on seismic surface waves, *Geophys. J. Int.,* **168,** 109–132.

Ge, S. & Saar, M.O., 2022. Review: induced seismicity during geoenergy development—a hydromechanical perspective, *J. geophys. Res.,* **127**(3), doi:10.1029/2021JB023141.

Gong, J.H. & McGuire, J.J., 2022. Waveform signatures of earthquakes located close to the subducted Gorda Plate interface, *Bull. seism. Soc. Am.,* **112,** 2440–2453.

Greenfield, T., Keir, D., Kendall, J.-M. & Ayele, A., 2019. Low-frequency earthquakes beneath Tullu Moye volcano, Ethiopia, reveal fluid pulses from shallow magma chamber, *Earth planet. Sci. Lett.,* **526,** doi:10.1016/j.epsl.2019.115782.

Harrington, R.M. & Brodsky, E.E., 2007. Volcanic hybrid earthquakes that are brittle-failure events, *Geophys. Res. Lett.,* **34**(6), doi:10.1029/2006GL028714.

Hu, H., Li, A. & Zavala-Torres, R., 2017. Long-period long-duration seismic events during hydraulic fracturing: implications for tensile fracture development, *Geophys. Res. Lett.,* **44,** 4814–4819.

Hung, R.J., Ma, K.F., Song, T.R.A., Lin, Y.Y. & Weingarten, M., 2022. Observation of temporal variations in seismic anisotropy within an active Fault-zone revealed from the Taiwan Chelungpu-Fault Drilling project borehole seismic array, *J. geophys. Res.,* **127**(4), doi:10.1029/2021JB023050.

Kita, S., Nakajima, J., Hasegawa, A., Okada, T., Katsumata, K., Asano, Y. & Kimura, T., 2014. Detailed seismic attenuation structure beneath Hokkaido, northeastern Japan: arc-arc collision process, arc magmatism, and seismotectonics, *J. geophys. Res.,* **119,** 6486–6511.

Lei, X., Huang, D., Su, J., Jiang, G., Wang, X., Wang, H., Guo, X. & Fu, H., 2017. Fault reactivation and earthquakes with magnitudes of up to Mw4.7 induced by shale-gas hydraulic fracturing in Sichuan Basin, China, *Sci. Rep.,* **7,** doi:10.1038/s41598-017-08557-y.

Lei, X., Su, J. & Wang, Z., 2020. Growing seismicity in the Sichuan Basin and its association with industrial activities, *Sci. China Earth Sci.,* **63,** 1633–1660.

Liu, G. *et al.* 2023. Detailed imaging of a seismogenic fault that potentially induced the two 2019 Weiyuan moderate earthquakes in the Sichuan Basin, China, *Seismol. Soc. Am.,* **94,** 1379–1391.

Liu, Q. & Gu, Y., 2012. Seismic imaging: from classical to adjoint tomography, *Tectonophysics,* **566-567,** 31–66.

Liu, Y.Y., Ma, X.H., Zhang, X.W., Wei, G., Kang, L.X., Yu, R.Z. & Sun, Y.P., 2021b. Shale gas well flowback rate prediction for Weiyuan field based on a deep learning algorithm, *J. Petrol. Sci. Eng.,* **203,** doi:10.1016/j.petrol.2021.108637.

Liu Yang, Y. *et al.* 2021a. Tectonic evolution of the Sichuan Basin, Southwest China, *Earth Sci. Rev.,* **213**(10), doi:10.1016/j.earscirev.2020.103470.

Long, F., Zhang, Z., Qi, Y., Liang, M., Ruan, X., Wu, W., Jiang, G. & Zhou, L., 2020. Three dimensional velocity structure and accurate earthquake location in Changning–Gongxian area of southeast Sichuan, *Earth planet. Phys.,* **4,** 1–15.

Luan, Y., Yang, H., Wang, B., Yang, W., Wang, W., Yang, J. & Li, X., 2022. Time-lapse monitoring of daily velocity changes in Binchuan, southwestern China, using large-volume air-gun source array data, *Seismol. Res. Lett.,* **93,** 914–930.

Mahani, A.B., Schultz, R., Kao, H., Walker, D., Johnson, J. & Salas, C., 2017. Fluid injection and seismic activity in the northern Montney play, British Columbia, Canada, with special reference to the 17 August 2015 M w 4.6 induced earthquake, *Bull. seism. Soc. Am.,* **107,** 542–552.

Makhanov, K., Habibi, A., Dehghanpour, H. & Kuru, E., 2014. Liquid uptake of gas shales: a workflow to estimate water loss during shut-in periods after fracturing operations, *J. Unconv. Oil Gas Res.,* **7,** 22–32.

Maxwell, S. & Urbancic, T., 2005. The potential role of passive seismic monitoring for real-time 4D reservoir characterization, *SPE Reserv. Eval. Eng.,* **8,** 70–76.

Miyazawa, M. & Kato, M., 2004. On interpolation functions in traveltime tomography, *Geophys. J. Int.,* **158,** 169–178.

Muller, T.M., Gurevich, B. & Lebedev, M., 2010. Seismic wave attenuation and dispersion resulting from wave-induced flow in porous rocks—a review, *Geophysics,* **75,** 75A147–75A164.

Murphy, W.F., 1982. Effects of partial water saturation on attenuation in Massilon sandstone and Vycor porous glass, *J. acoust. Soc. Am.,* **71,** 1458–1468.

Niyogi, S., Ghosh, A., Kumar, A. & Hammack, R.W., 2023. Tremor signals during fluid injection are generated by fault slip, *Science,* **381,** 553–558.

Saenger, E.H. *et al.* 2009. A passive seismic survey over a gas field: analysis of low-frequency anomalies, *Geophysics,* **74,** O29–O40.

Sebastiano, D., Francesco, P., Salvatore, M., Roberto, I., Antonella, P., Giuseppe, L., Pauline, G. & Daniela, F., 2019. Ambient noise techniques to study near-surface in particular geological conditions: a brief review, in *Innovation in Near-Surface GeophysicsInstrumentation, Application, and Data Processing Methods,* pp. 419–460, eds Persico, R., Piro, S. & Linford, N., Elsevier.

Shapiro, S.A., Parotidis, M., Rentsch, S. & Rothert, E., 2004. Reservoir characterization using passive seismic monitoring: physical fundamentals and road ahead, in *SEG Technical Program Expanded Abstracts 2004,* pp. 2541–2544, Society of Exploration Geophysicists.

She, Y.Y., Yao, H.J., Yang, H.F., Wang, J.J. & Feng, J.K., 2022. Constraining the depth extent of low-velocity zone along the Chenghai Fault by dense array ambient noise interferometry and horizontal-to-vertical spectral ratio, *Tectonophysics,* **827,** doi:10.1016/j.tecto.2022.229265.

Sheng, M., Chu, R., Peng, Z., Wei, Z., Zeng, X., Wang, Q. & Wang, Y., 2022. Earthquakes triggered by fluid diffusion and boosted by fault reactivation in Weiyuan, China due to hydraulic fracturing, *J. geophys. Res.,* **127**(5), doi:10.1029/2021JB022963.

Simm, R., Bacon, M. & Bacon, M., 2014. *Seismic Amplitude: An Interpreter's Handbook,* Cambridge Univ. Press.

Song, J. & Yang, H., 2022. Seismic site response inferred from records at a dense linear array across the Chenghai fault Zone, Binchuan, Yunnan, *J. geophys. Res.,* **127**(1), doi:10.1029/2021JB022710.

Song, Z., Tan, Y.J. & Roman, D.C., 2023. Deep long-period earthquakes at Akutan volcano from 2005 to 2017 better track magma influxes compared to volcano-tectonic earthquakes, *Geophys. Res. Lett.,* **50**(10), doi:10.1029/2022GL101987.

Tan, Y. *et al.* 2023. Tomographic evidences for hydraulic fracturing induced seismicity in the Changning shale gas field, southern Sichuan Basin, China, *Earth planet. Sci. Lett.,* **605,** doi:10.1016/j.epsl.2023.118021.

Tian, Z., Shi, L. & Qiao, L., 2015. Problems in the wellbore integrity of a shale gas horizontal well and corresponding countermeasures, *Nat. Gas Indust., B,* **2,** 522–529.

Tselentis, G.-A., Martakis, N., Paraskevopoulos, P. & Lois, A., 2011. High-resolution passive seismic tomography for 3D velocity, Poisson's ratio ν, and P-wave quality QP in the Delvina hydrocarbon field, southern AlbaniaTselentis et al. PST for 3D velocity, ν and QP, *Geophysics,* **76,** B89–B112.

Wang, B., Harrington, R.M., Liu, Y., Kao, H. & Yu, H., 2020a. A study on the largest hydraulic-fracturing-induced earthquake in Canada: observations and static stress-drop estimation, *Bull. seism. Soc. Am.,* **110,** 2283–2294.

Wang, M., Yang, H., Fang, L., Han, L., Jia, D., Jiang, D. & Yan, B., 2020b. Shallow faults reactivated by hydraulic fracturing: the 2019 Weiyuan earthquake sequences in Sichuan, China, *Seismol. Res. Lett.,* **91,** 3171–3181.

Wang, R., Gu, Y.J., Schultz, R., Zhang, M. & Kim, A., 2017. Source characteristics and geological implications of the January 2016 induced earthquake swarm near Crooked Lake, Alberta, *Geophys. J. Int.,* **210,** 979–988.

Wong, J.W., Wing Zi, J., Yang, H. & Jinrong Su, A., 2021. Spatial-temporal evolution of injection induced earthquakes in Weiyuan area by machine-learning phase picker and waveform cross-correlation, *Earth and Planetary Physics,* **5,** 0–0.

Yang, H., Li, Z., Peng, Z., Ben-Zion, Y. & Vernon, F., 2014. Low-velocity zones along the San Jacinto Fault, Southern California, from body waves recorded in dense linear arrays, *J. geophys. Res.,* **119,** 8976–8990.

Yang, H. & Yao, S., 2021. Shallow destructive earthquakes, *Earthq. Sci.,* **34,** 15–23.

Yang, H., Zhou, P., Fang, N., Zhu, G., Xu, W., Su, J., Meng, F. & Chu, R., 2020. A shallow shock: the 25 February 2019 ML 4.9 earthquake in the Weiyuan Shale Gas Field in Sichuan, China, *Seismol. Res. Lett.,* **91,** 3182–3194.

Yang, H.F. & Zhu, L.P., 2010. Shallow low-velocity zone of the San Jacinto fault from local earthquake waveform modelling, *Geophys. J. Int.,* **183,** 421–432.

Yang, W., Wang, B.S., Yuan, S.Y. & Ge, H.K., 2018. Temporal variation of seismic-wave velocity associated with groundwater level observed by a downhole airgun near the Xiaojiang Fault Zone, *Seismol. Res. Lett.,* **89,** 1014–1022.

Yang, Y., Yang, H. & Zi, J., 2023. Stress transfer outpaces injection-induced aseismic slip and triggers seismicity. Research Square Platform LLC.

Yi, G.X., Long, F., Liang, M.J., Zhao, M. & Wang, S.W., 2020. Geometry and tectonic deformation of seismogenic structures in the Rongxian-Weiyuan-Zizhong region, Sichuan Basin: insights from focal mechanism solutions, *Chinese J. Geophys.,* **63,** 3275–3291.

Yin, C.-S., Batzle, M.L. & Smith, B.J., 1992. Effects of partial liquid/gas saturation on extensional wave attenuation in Berea sandstone, *Geophys. Res. Lett.,* **19,** 1399–1402.

Yu, H., Harrington, R.M., Kao, H., Liu, Y. & Wang, B., 2021. Fluid-injection-induced earthquakes characterized by hybrid-frequency waveforms manifest the transition from aseismic to seismic slip, *Nat. Commun.,* **12,** doi:10.1038/s41467-021-26961-x.

Yu, R., Qian, J., Liu, L., Zha, H. & Li, N., 2022. Microseismic precursors of coal mine water inrush characterized by different waveforms manifest as dry to wet fracturing, *Int. J. Environ. Res. Public Health,* **19**(21), doi:10.3390/ijerph192114291.

Zeng, Q., CHU, R., SHENG, M. & WEI, Z., 2020. Seismic ambient noise tomography for shallow velocity structures beneath Weiyuan, Sichuan, *Chinese J. Geophys.,* **63,** 944–955.

Zhai, H., Chang, X., Wang, Y., Xue, Z., Lei, X. & Zhang, Y., 2017. Sensitivity analysis of seismic velocity and attenuation variations for Longmaxi Shale during hydraulic fracturing testing in laboratory, *Energies,* **10**(9), doi:10.3390/en10091393.

Zhang, B., Lei, J. & Zhang, G., 2020. Seismic evidence for influences of deep fluids on the 2019 Changning Ms 6.0 earthquake, Sichuan basin, SW China, *J. Asian Earth Sci.,* **200,** doi:10.1016/j.jseaes.2020.104492.

Zhang, H., Sarkar, S., Toksöz, M.N., Kuleli, H.S. & Al-Kindy, F., 2009. Passive seismic tomography using induced seismicity at a petroleum field in Oman, *Geophysics,* **74,** WCB57–WCB69.

Zhang, J., Yang, H., Zi, J., Su, J. & Chen, X., 2024. An improved estimation of stress drop and its application on induced earthquakes in theWeiyuan Shale Gas Field in China, *Geophys. J. Int.* **236**(3), 1785–1803.

Zhang, Z., Deng, Y., Qiu, H., Peng, Z. & Liu-Zeng, J., 2022. High-resolution imaging of Fault zone structure along the creeping section of the Haiyuan Fault, NE Tibet, from data recorded by dense seismic arrays, *J. geophys. Res.,* **127**(9), doi:10.1029/2022JB024468.

Zhu, G., Yang, H., Lin, J., Zhou, Z., Xu, M., Sun, J. & Wan, K., 2019. Along-strike variation in slab geometry at the southern Mariana subduction zone revealed by seismicity through ocean bottom seismic experiments, *Geophys. J. Int.,* **218,** 2122–2135.

Zhu, Y.P., Tsvankin, I., Dewangan, P. & van Wijk, K., 2007. Physical modeling and analysis of P-wave attenuation anisotropy in transversely isotropic media, *Geophysics,* **72,** D1–D7.

Zi, J., Yang, H., Su, J. & Chen, L., 2023. Structural constraints of induced earthquakes in the Weiyuan Shale Gas Field revealed by high-resolution body-wave tomography and earthquake relocation, *Tectonophysics,* **864,** doi:10.1016/j.tecto.2023.230007.